

OCT-based crystalline lens topography in accommodating eyes

Pablo Pérez-Merino,* Miriam Velasco-Ocana, Eduardo Martínez-Enriquez, and Susana Marcos

Instituto de Óptica "Daza de Valdés," Consejo Superior de Investigaciones Científicas, C/Serrano 121, 28006 Madrid, Spain

*p.perez@io.cfmac.csic.es

Abstract: Custom Spectral Domain Optical Coherence Tomography (SD-OCT) provided with automatic quantification and distortion correction algorithms was used to measure anterior and posterior crystalline lens surface elevation in accommodating eyes and to evaluate relationships between anterior segment surfaces. Nine young eyes were measured at different accommodative demands. Anterior and posterior lens radii of curvature decreased at a rate of 0.78 ± 0.18 and 0.13 ± 0.07 mm/D, anterior chamber depth decreased at 0.04 ± 0.01 mm/D and lens thickness increased at 0.04 ± 0.01 mm/D with accommodation. Three-dimensional surface elevations were estimated by subtracting best fitting spheres. In the relaxed state, the spherical term accounted for most of the surface irregularity in the anterior lens (47%) and astigmatism (70%) in the posterior lens. However, in accommodated lenses astigmatism was the predominant surface irregularity (90%) in the anterior lens. The RMS of high-order irregularities of the posterior lens surface was statistically significantly higher than that of the anterior lens surface ($\times 2.02$, $p < 0.0001$). There was significant negative correlation in vertical coma (Z_3^{-1}) and oblique trefoil (Z_3^{-3}) between lens surfaces. The astigmatic angle showed high degree of alignment between corneal surfaces, moderate between corneal and anterior lens surface (~ 27 deg), but differed by ~ 80 deg between the anterior and posterior lens surfaces (including relative anterior/posterior lens astigmatic angle shifts, 10-20 deg).

© 2015 Optical Society of America

OCIS codes: (110.4500) Optical coherence tomography; (120.6650) Surface measurements, figure; (110.6880) Three-dimensional image acquisition; (100.2960) Image analysis; (330.7327) Visual optics, ophthalmic instrumentation; (330.7322) Visual optics, accommodation; (200.4560) Visual optics, aging changes.

References and links

1. W. N. Charman, "Physiological optics in 2008: standing on Helmholtz's shoulders," *Ophthalmic Physiol. Opt.* **29**(3), 209–210 (2009).
2. G. Smith, B. K. Pierscionek, and D. A. Atchison, "The optical modelling of the human lens," *Ophthalmic Physiol. Opt.* **11**(4), 359–369 (1991).
3. L. F. Garner, "Calculation of the radii of curvature of the crystalline lens surfaces," *Ophthalmic Physiol. Opt.* **17**(1), 75–80 (1997).
4. G. K. Hung, K. J. Ciuffreda, and M. Rosenfield, "Proximal contribution to a linear static model of accommodation and vergence," *Ophthalmic Physiol. Opt.* **16**(1), 31–41 (1996).
5. D. Stone, S. Mathews, and P. B. Kruger, "Accommodation and chromatic aberration: effect of spatial frequency," *Ophthalmic Physiol. Opt.* **13**(3), 244–252 (1993).
6. N. López-Gil, I. Iglesias, and P. Artal, "Retinal image quality in the human eye as a function of the accommodation," *Vision Res.* **38**(19), 2897–2907 (1998).
7. J. Liang and D. R. Williams, "Aberrations and retinal image quality of the normal human eye," *J. Opt. Soc. Am. A* **14**(11), 2873–2883 (1997).

8. J. C. He, S. A. Burns, and S. Marcos, "Monochromatic aberrations in the accommodated human eye," *Vision Res.* **40**(1), 41–48 (2000).
9. E. Gamba, Y. Wang, J. Yuan, P. B. Kruger, and S. Marcos, "Dynamic accommodation with simulated targets blurred with high order aberrations," *Vision Res.* **50**(19), 1922–1927 (2010).
10. D. A. Atchison, "Accommodation and presbyopia," *Ophthalmic Physiol. Opt.* **15**(4), 255–272 (1995).
11. A. Glasser and M. C. Campbell, "Presbyopia and the optical changes in the human crystalline lens with age," *Vision Res.* **38**(2), 209–229 (1998).
12. P. Rosales, M. Dubbelman, S. Marcos, and R. van der Heijde, "Crystalline lens radii of curvature from Purkinje and Scheimpflug imaging," *J. Vis.* **6**(10), 1057–1067 (2006).
13. P. Rosales and S. Marcos, "Phakometry and lens tilt and decentration using a custom-developed Purkinje imaging apparatus: validation and measurements," *J. Opt. Soc. Am. A* **23**(3), 509–520 (2006).
14. P. Rosales and S. Marcos, "Pentacam Scheimpflug quantitative imaging of the crystalline lens and intraocular lens," *J. Refract. Surg.* **25**(5), 421–428 (2009).
15. J. E. Koretz, S. A. Strenk, L. M. Strenk, and J. L. Semmlow, "Scheimpflug and high-resolution magnetic resonance imaging of the anterior segment: a comparative study," *J. Opt. Soc. Am. A* **21**(3), 346–354 (2004).
16. M. Dubbelman and G. L. Van der Heijde, "The shape of the aging human lens: curvature, equivalent refractive index and the lens paradox," *Vision Res.* **41**(14), 1867–1877 (2001).
17. S. Kasthurirangan, E. L. Markwell, D. A. Atchison, and J. M. Pope, "MRI study of the changes in crystalline lens shape with accommodation and aging in humans," *J. Vis.* **11**(3), 19 (2011).
18. M. Ruggeri, S. R. Uhlhorn, C. De Freitas, A. Ho, F. Manns, and J. M. Parel, "Imaging and full-length biometry of the eye during accommodation using spectral domain OCT with an optical switch," *Biomed. Opt. Express* **3**(7), 1506–1520 (2012).
19. A. Neri, M. Ruggeri, A. Protti, R. Leaci, S. A. Gandolfi, and C. Macaluso, "Dynamic imaging of accommodation by swept-source anterior segment optical coherence tomography," *J. Cataract Refract. Surg.* **41**(3), 501–510 (2015).
20. L. Leng, Y. Yuan, Q. Chen, M. Shen, Q. Ma, B. Lin, D. Zhu, J. Qu, and F. Lu, "Biometry of anterior segment of human eye on both horizontal and vertical meridians during accommodation imaged with extended scan depth optical coherence tomography," *PLoS One* **9**(8), e104775 (2014).
21. J. C. He and J. Wang, "Measurement of wavefront aberrations and lens deformation in the accommodated eye with optical coherence tomography-equipped wavefront system," *Opt. Express* **22**(8), 9764–9773 (2014).
22. J. Birkenfeld, A. de Castro, S. Ortiz, D. Pascual, and S. Marcos, "Contribution of the gradient refractive index and shape to the crystalline lens spherical aberration and astigmatism," *Vision Res.* **86**, 27–34 (2013).
23. A. Roorda and A. Glasser, "Wave aberrations of the isolated crystalline lens," *J. Vis.* **4**(4), 250–261 (2004).
24. P. Artal, A. Guirao, E. Berrio, and D. R. Williams, "Compensation of corneal aberrations by the internal optics in the human eye," *J. Vis.* **1**(1), 1–8 (2001).
25. J. E. Kelly, T. Mihashi, and H. C. Howland, "Compensation of corneal horizontal/vertical astigmatism, lateral coma, and spherical aberration by internal optics of the eye," *J. Vis.* **4**(4), 262–271 (2004).
26. I. Grulkowski, M. Gora, M. Szkulmowski, I. Gorczynska, D. Szlag, S. Marcos, A. Kowalczyk, and M. Wojtkowski, "Anterior segment imaging with Spectral OCT system using a high-speed CMOS camera," *Opt. Express* **17**(6), 4842–4858 (2009).
27. S. Ortiz, P. Pérez-Merino, S. Durán, M. Velasco-Ocana, J. Birkenfeld, A. de Castro, I. Jiménez-Alfaro, and S. Marcos, "Full OCT anterior segment biometry: an application in cataract surgery," *Biomed. Opt. Express* **4**(3), 387–396 (2013).
28. S. Ortiz, P. Pérez-Merino, E. Gamba, A. de Castro, and S. Marcos, "In vivo human crystalline lens topography," *Biomed. Opt. Express* **3**(10), 2471–2488 (2012).
29. S. Ortiz, D. Siedlecki, I. Grulkowski, L. Remon, D. Pascual, M. Wojtkowski, and S. Marcos, "Optical distortion correction in optical coherence tomography for quantitative ocular anterior segment by three-dimensional imaging," *Opt. Express* **18**(3), 2782–2796 (2010).
30. S. Ortiz, D. Siedlecki, P. Pérez-Merino, N. Chia, A. de Castro, M. Szkulmowski, M. Wojtkowski, and S. Marcos, "Corneal topography from spectral optical coherence tomography (sOCT)," *Biomed. Opt. Express* **2**(12), 3232–3247 (2011).
31. S. Ortiz, D. Siedlecki, L. Remon, and S. Marcos, "Three-dimensional ray tracing on Delaunay-based reconstructed surfaces," *Appl. Opt.* **48**(20), 3886–3893 (2009).
32. S. Ortiz, D. Siedlecki, L. Remon, and S. Marcos, "Optical coherence tomography for quantitative surface topography," *Appl. Opt.* **48**(35), 6708–6715 (2009).
33. A. de Castro, S. Ortiz, E. Gamba, D. Siedlecki, and S. Marcos, "Three-dimensional reconstruction of the crystalline lens gradient index distribution from OCT imaging," *Opt. Express* **18**(21), 21905–21917 (2010).
34. P. Pérez-Merino, S. Ortiz, N. Alejandro, I. Jiménez-Alfaro, and S. Marcos, "Quantitative OCT-based longitudinal evaluation of intracorneal ring segment implantation in keratoconus," *Invest. Ophthalmol. Vis. Sci.* **54**(9), 6040–6051 (2013).
35. E. Gamba, S. Ortiz, P. Pérez-Merino, M. Gora, M. Wojtkowski, and S. Marcos, "Static and dynamic crystalline lens accommodation evaluated using quantitative 3-D OCT," *Biomed. Opt. Express* **4**(9), 1595–1609 (2013).

36. S. R. Uhlhorn, D. Borja, F. Manns, and J. M. Parel, "Refractive index measurement of the isolated crystalline lens using optical coherence tomography," *Vision Res.* **48**(27), 2732–2738 (2008).
37. T. O. Salmon, R. W. West, W. Gasser, and T. Kenmore, "Measurement of refractive errors in young myopes using the COAS Shack-Hartmann aberrometer," *Optom. Vis. Sci.* **80**(1), 6–14 (2003).
38. K. Karnowski, B. J. Kaluzny, M. Szkulmowski, M. Gora, and M. Wojtkowski, "Corneal topography with high-speed swept source OCT in clinical examination," *Biomed. Opt. Express* **2**(9), 2709–2720 (2011).
39. M. Zhao, A. N. Kuo, and J. A. Izatt, "3D refraction correction and extraction of clinical parameters from spectral domain optical coherence tomography of the cornea," *Opt. Express* **18**(9), 8923–8936 (2010).
40. P. Pérez-Merino, S. Ortiz, N. Alejandre, A. de Castro, I. Jiménez-Alfaro, and S. Marcos, "Ocular and optical coherence tomography-based corneal aberrometry in keratoconic eyes treated by intracorneal ring segments," *Am. J. Ophthalmol.* **157**(1), 116–127 (2014).
41. P. R. Keller, M. J. Collins, L. G. Carney, B. A. Davis, and P. P. van Saarloos, "The relation between corneal and total astigmatism," *Optom. Vis. Sci.* **73**(2), 86–91 (1996).
42. M. C. Dunne, M. E. Elawad, and D. A. Barnes, "Measurement of astigmatism arising from the internal ocular surfaces," *Acta Ophthalmol. Scand.* **74**(1), 14–20 (1996).
43. P. Artal, E. Berrio, A. Guirao, and P. Piers, "Contribution of the cornea and internal surfaces to the change of ocular aberrations with age," *J. Opt. Soc. Am. A* **19**(1), 137–143 (2002).
44. T. Grosvenor, S. Quintero, and D. M. Perrigin, "Predicting refractive astigmatism: a suggested simplification of Javal's rule," *Am. J. Optom. Physiol. Opt.* **65**(4), 292–297 (1988).
45. M. Dubbelman, V. A. Sicam, and G. L. Van der Heijde, "The shape of the anterior and posterior surface of the aging human cornea," *Vision Res.* **46**(6-7), 993–1001 (2006).
46. M. Dubbelman, V. A. Sicam, and R. G. van der Heijde, "The contribution of the posterior surface to the coma aberration of the human cornea," *J. Vis.* **7**(10), 11–18 (2007).
47. M. Sun, J. Birkenfeld, A. de Castro, S. Ortiz, and S. Marcos, "OCT 3-D surface topography of isolated human crystalline lenses," *Biomed. Opt. Express* **5**(10), 3547–3561 (2014).
48. L. F. Garner and G. Smith, "Changes in equivalent and gradient refractive index of the crystalline lens with accommodation," *Optom. Vis. Sci.* **74**(2), 114–119 (1997).
49. A. de Castro, J. Birkenfeld, B. Maceo, F. Manns, E. Arrieta, J. M. Parel, and S. Marcos, "Influence of shape and gradient refractive index in the accommodative changes of spherical aberration in nonhuman primate crystalline lenses," *Invest. Ophthalmol. Vis. Sci.* **54**(9), 6197–6207 (2013).
50. J. Birkenfeld, A. de Castro, and S. Marcos, "Contribution of shape and gradient refractive index to the spherical aberration of isolated human lenses," *Invest. Ophthalmol. Vis. Sci.* **55**(4), 2599–2607 (2014).
51. P. Rosales, M. Wendt, S. Marcos, and A. Glasser, "Changes in crystalline lens radii of curvature and lens tilt and decentration during dynamic accommodation in rhesus monkeys," *J. Vis.* **8**(18), 11–12 (2008).

1. Introduction

The optical components of the eye are the cornea and the crystalline lens; they must be transparent and have appropriate shape and refractive indices for providing an optimal retinal image. The cornea accounts for most of the optical refractive power, while the crystalline lens provides approximately one third of the total static refractive power of the eye and is the responsible for the focusing ability in young eyes (process known as accommodation) [1–9].

During accommodation, the ciliary muscle contracts, relaxing the tension on the zonular fibers and changing the crystalline lens geometry, primarily increasing the curvature of its surfaces. These changes overall contribute to additional ~10 diopters (D) of refraction in the young adult eye; however, by age 45 most of the accommodation amplitude is lost (process known as presbyopia) [10,11].

Despite the important contribution of the crystalline lens to the optical quality of the eye, due to its inaccessibility, knowledge of *in vivo* geometrical parameters of the crystalline lens (relaxed or accommodated) is limited. Information on the crystalline lens provided by commercial instruments is generally limited to axial properties (e.g., crystalline lens thickness). There are also numerous reports in the literature reporting lens radii of curvature, measured generally with adapted commercial or custom-developed instruments: Purkinje imaging [12,13], Scheimpflug camera [14–16], Magnetic Resonance Imaging (MRI) [17] and, recently, Optical Coherence Tomography (OCT) [18–21].

Different studies have also reported the change in the optics of the crystalline lens with accommodation, describing changes in spherical aberration (towards more negative

values), and an increase in astigmatism and coma [6–9]. Lens aberrations have been measured either *ex vivo* (using laser ray tracing [22] or Hartmann-Shack [23]), or *in vivo* by subtracting corneal aberrations from total aberrations [24,25]. However, although aberrometers allow measuring the relative contribution of the crystalline lens to the optics of the eye, the relative contribution of the lens surfaces themselves to aberrations is still poorly understood. In particular, most data on anterior and posterior lens surfaces come from single cross-sections, not revealing topographic features of the lens.

A deeper analysis of lens shape and geometry is crucial for understanding its optical properties, and will help to understand (1) the compensatory role of the crystalline lens aberrations to corneal aberrations, (2) the mechanisms of accommodation of the crystalline lens, (3) the role of the crystalline lens in the development of refractive errors (e.g., myopia), (4) the age-related changes of the crystalline lens optics and (5) will help to increase the predictability of intraocular lens (IOL) implantation.

In this study, we present, for the first time to our knowledge, 3-D surface elevation crystalline lens changes with accommodation *in vivo*. We specifically explored the role of astigmatism and high-order irregularities of all anterior segment surfaces (cornea and lens) and their relationship.

2. Material and methods

2.1. Subjects

Nine eyes from seven young subjects (mean age: 31 ± 3.1 y.o) were studied. Refractive errors ranged between -5.25 to $+0.75$ D sphere and -1.25 to 0 D cylinder (Table 1). Subjects signed a consent form approved by the Institutional Review Boards after they had been informed on the nature and possible consequences of the study, in accordance to the tenets of the Declaration of Helsinki.

Table 1. Individual refractive profile (age and refractive error)

	Age (y.o)	Sphere (D)	Cylinder (D) / axis (deg)
S#1 (OS)	29	-0.5	-0.5 / 20
S#2 (OD)	32	-1.5	-0.5 / 80
S#2 (OS)	32	-1.5	-0.25 / 110
S#3 (OD)	26	-2.5	-0.75 / 150
S#4 (OS)	30	-1.5	-0.25 / 50
S#5 (OS)	36	-5.25	-1.00 / 170
S#6 (OD)	31	-4.25	-1.25 / 175
S#6 (OS)	31	-4.25	-1.25 / 180
S#7 (OS)	33	+0.75	-0.5 / 80

2.2. OCT system

The SD-OCT instrument, and a set of algorithms for image processing and distortion correction (fan and optical) to obtain anterior and posterior corneal and crystalline lens topographies from OCT images have been described in detail in previous publications [26–32]. Briefly, the set-up is based on a fiber-optics Michelson interferometer configuration with a superluminescent diode ($\lambda_0 = 840$ nm, $\Delta\lambda = 50$ nm) as a light source, and a spectrometer consisting of a volume diffraction grating and a CMOS camera as a detector. The effective acquisition speed is 25000 A-Scans/s. The axial range is 7 mm in depth, resulting in a theoretical pixel resolution of 3.4 μm . The nominal axial resolution, as given by the coherence length of the source, is 6.9 μm in tissue.

For the purposes of this study, an external accommodative channel was incorporated to the OCT. A Badal system mounted on a motorized stage (VXM-1, Velmex) was used for compensating defocus and for inducing accommodation. The fixation stimulus consists of a 20/25 white Snellen E-letter presented in a black background on a Digital-Light-Processing (DLP) picoprojector (854x480 pixels, Philips NV, Amsterdam,

Netherlands; 55 lum) subtending a 5-arcmin visual angle. Two neutral filters (ND 16) were placed after the picoprojector to produce an average luminance of $\sim 30\text{cd/m}^2$ in an otherwise dark environment. The OCT axis was aligned with the pupillary axis by moving the fixation stimulus in 5 pixels-steps horizontally and vertically until the iris appeared flat in the preview OCT horizontal and vertical cross-sections, so all measurements were acquired when both OCT and pupillary axis were aligned.

2.3. Experimental protocols

The subjects viewed the stimulus monocularly, with the contralateral eye covered with a patch during the measurements. Measurements were collected in 11×11 mm area and consisted of a collection of 50 B-scans composed by 300 A-scans. The total acquisition time of a 3-D data set was 0.6 seconds. These parameters showed a good balance between time acquisition and resolution for further Zernike fit of the surfaces. The anterior segment of the eye was imaged while stimulating accommodation from 0 to 6 D, in 1.5-D steps. Images containing artifacts (i.e., eyelids) which precluded corneal and lens surface analysis within the optical zone were excluded. Five repeated measurements were collected in each condition after inducing mydriasis with one drop of phenylephrine, which allowed larger pupils without paralyzing the ciliary muscle.

The specifications of the spectrometer and light source do not allow sufficient axial range to capture all anterior segment surfaces in a single acquisition. To solve that, three sets of 3-D images were captured sequentially at 5 seconds after blinking: (1) cornea, (2) anterior lens and (3) posterior lens, rapidly shifting axially the plane of focus; all 3-D sets of data contained the iris.

2.4. OCT image processing

In previous studies, we described image-processing tools for distortion correction, denoising, segmentation and merging of volumes [27–30,32–35]. The quantification capabilities of the OCT have been validated *ex vivo* with artificial model eyes with known dimensions, and *in vivo* comparing with other imaging techniques (videokeratography, Scheimpflug and non-contact profilometry) [30]. In this study we incorporated improved signal processing algorithms, including a simpler and more robust approach to automatic surface segmentation. For every B-scan, simple uni-modal thresholding and morphological operations on the resulting binary image were used to generate masks, which allowed identification of signal of interest in the different eye structures. Segmentation algorithms use properties of these masks (i.e. centroid positions) and *a-priori* knowledge on the measurements (i.e. relative position of iris and cornea). Finally, an AND operation between labeled masks and edges (obtained using a Canny detector) is performed in order to obtain the layers of interest.

Images of the cornea, anterior lens and posterior lens were merged for further registration: (1) the corneal image was inverted (since, for efficiency in the focus range shift, the cornea was acquired in the opposite side of the Fourier transform) and then (2) the 3-D volumes of the anterior cornea/iris and posterior lens/iris were shifted to the fixed reference in order to superimpose these volumes to the anterior lens/iris volume (Fig. 1).

Distortion correction (fan and optical) algorithms were applied on the merged volumes for quantification by using 3-D ray tracing routines [29–32]. The corneal refractive index was taken as 1.376, the aqueous humor refractive index as 1.336, and the crystalline lens refractive index was obtained from the age-dependent average refractive index expression derived by Uhlhorn et al. [36]. Figure 2 illustrates the change in anterior segment biometric and geometrical parameters following transformation of optical paths to distances and distortion corrections. For example, distortions produced errors of 38%–17% in the estimates of anterior and posterior lens radii of curvature.

The optical zone diameter reduced across surfaces due to refraction. The mean diameters in the different surfaces were 6.32 ± 0.07 mm at the anterior cornea, 6.17 ± 0.06 mm at the posterior cornea, 5.47 ± 0.11 mm at the anterior cornea, and 4.74 ± 0.12 mm at the anterior cornea in the relaxed state (mean \pm SD for all eyes). For comparison of the surface elevation maps, the analysis was performed for a constant pupil of 4-mm diameter (common to all subjects and surfaces, and free of edge artifacts).

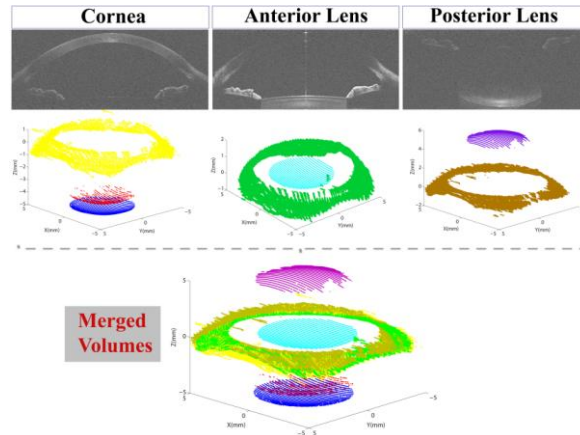


Fig. 1. Illustration of the acquisition of an individual data collection of three volume acquisitions and merging to obtain a 3-D full anterior segment volume.

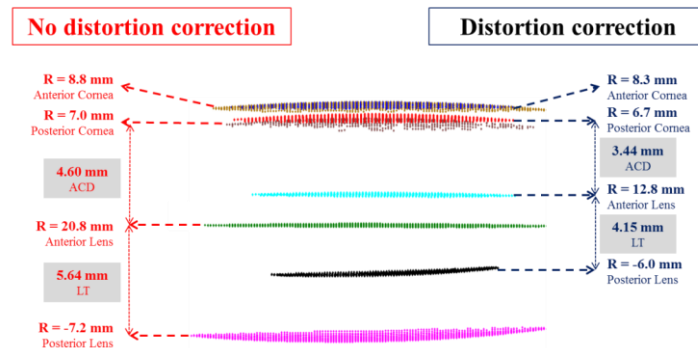


Fig. 2. Illustration of the effect of distortion correction on the anterior segment surfaces in S#1 (OS). Left data: from optical paths, without distortion correction; right data: distortion correction.

All signal processing algorithms run completely automatically with no need of user interaction. Full computational processing time per eye was 14.6 s (Intel Xeon CPU@3.5 GHz processor, 8GB RAM).

2.5. Biometric, geometric and surface elevation changes with accommodation

The geometrical distances between ocular elements in the anterior segment were taken from the apex positions: (1) anterior chamber depth (ACD), distance between the posterior corneal apex and the anterior lens surface apex, and (2) lens thickness (LT), distance between the anterior and posterior lens apex (Fig. 3).

Corneal and lens segmented surfaces were first fitted by spheres, and their radii of curvature estimated. Corneal and lens surface elevations were obtained by subtraction of the best fitting spheres from the segmented surfaces. Both, corneal and lens surfaces were

fitted by Zernike polynomial expansions (6th order; note that these Zernike coefficients describe surface elevations, and not wave aberrations).

Descriptive parameters of the surface elevation maps include individual surface Zernike coefficients, the Root Mean Square (RMS) for all high order coefficients (excluding tilt, defocus and astigmatism) and the RMS of the combination of some terms (RMS astigmatism, RMS trefoil and RMS coma).

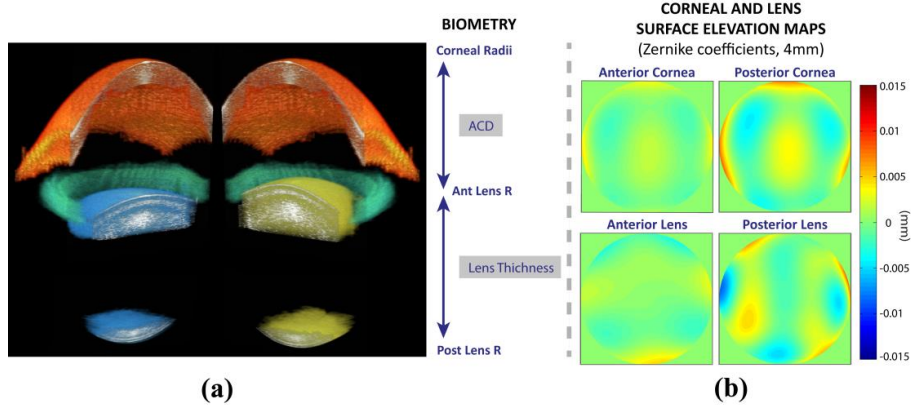


Fig. 3. (a) Examples of 3-D images in S#2 (OD) relaxed (left) and for 6 D of accommodative demand (right). (b) Corneal (up) and crystalline lens (down), anterior (left) and posterior (right) surface elevation maps in S#2 (OD) relaxed accommodation. Data are for 4 mm.

2.6. Accommodative response

The accommodative response was estimated from the changes in the anterior segment biometry data (radii, ACD and LT) with accommodation. A schematic eye model in paraxial approximation (considering all refractive indices of the eye) was used to analyze the refractive change of the eye.

$$P_C = \frac{n_h - 1}{R_c}; \quad P_L = (n_l - n_h) \left(\frac{1}{R_a} - \frac{1}{R_p} \right) + \frac{(n_l - n_h)^2}{n_l} \frac{LT}{R_a R_p} \quad (1)$$

$$P = P_C + P_L - \frac{ACD * P_C * P_L}{n_h} + \frac{(n_l - n_h) * LT * P_C}{n_l * R_p} \quad (2)$$

where P , P_C and P_L are the power of the eye, cornea and lens, n_h and n_l are the refractive indexes of the aqueous humor and the lens, and R_c , R_a and R_p are the radii of curvature of the cornea, anterior lens and posterior lens

2.7. Corneal and lens surface astigmatism axis

The corneal and lens surfaces astigmatism (C) and angle (α) were obtained from the surface elevation astigmatism Zernike coefficients using Eq. (3):

$$J_0 = \frac{-2\sqrt{6}C_2^2}{R^2}; \quad J_{45} = \frac{-2\sqrt{6}C_2^{-2}}{R^2}; \quad C = -2\sqrt{J_0^2 + J_{45}^2}; \quad \alpha = \frac{1}{2} \arctan \frac{J_{45}}{J_0} \quad \text{Eq.(3)}$$

Where J_0 and J_{45} are the surface power at axis $\alpha = 0$ and 45 degrees respectively, and r the pupil radius (2-mm, in this study). To ensure that the minus-cylinder axis is a value between 0 and 180 degrees we consider the following: If $J_0 < 0$, then meridian = axis + 90 degrees; if $J_0 = 0$, and if $J_{45} < 0$, then meridian = 135 degrees; if $J_0 = 0$, and if $J_{45} > 0$, then

meridian = 45 degrees; if $J_0 > 0$, and if $J_{45} \leq 0$, then meridian = axis + 180 degrees; if $J_0 > 0$, and if $J_{45} > 0$, then meridian = axis [37].

We represent anterior and posterior corneal and lens surface astigmatism data in a power vector graph. The length of the vectors represents the calculated magnitude of surface astigmatism (in diopters) and the direction of the vectors allows estimating the relative angle between anterior and posterior corneal and lens astigmatism axis. All vectors were represented in a polar coordinate system.

2.8. Spatial resolution and accuracy considerations

The effective axial resolution, the effect of lateral sampling, and the robustness of the merging algorithm were investigated, as they all play a role in the accuracy of the lens surface elevation estimates. A simulation on virtual surfaces with added white noise of standard deviation equal to the nominal axial resolution (1000 realizations), revealed differences between the original-correct-surface and the noisy surfaces of 2.4 μm (RMS surface elevation) and 0.28 μm (RMS of the Zernike coefficients). Therefore the error caused by the axial resolution limit is around half to that given by the nominal OCT axial resolution. Also, a simulation using 500 random realistic surfaces of 300 A-Scans x 300 B-Scans in a 5x5 mm which were then subsampled by a sampling factor of 6 in the y-coordinate (as in our measurement configuration, 50 B-Scans) showed that the RMS error between the generated and the subsampled surfaces was below 0.3 μm , demonstrating a low impact of sampling in the lateral resolution of our measurements. Finally, we evaluated the accuracy and robustness of the merging methodology by removing a percentage of points of the iris (randomly taken from a uniform distribution), and we compared the estimated center point of the complete and the subsampled iris. The mean estimation error was below 2 μm for x_0 , y_0 and z_0 if we removed 80% of the iris points.

2.9. Statistics

The changes in lens surfaces with accommodation were analyzed using an analysis of variance (ANOVA; general linear model for repeated measurements). Significant levels (ANOVA and pair-wise two tailed comparison t-test) were set at $p < 0.05$. The statistical significant levels were adjusted by a Bonferroni correction. The statistical tests were performed using SPSS software (SPSS, Inc., Chicago, Illinois).

3. Results

3.1. Anterior and posterior lens surface elevation (relaxed state)

Figure 4 shows anterior and posterior surface elevation maps (3rd and higher-order terms) and Fig. 5 shows the Zernike terms (also including astigmatism), in all eyes in the relaxed state. The posterior lens shape generally shows higher magnitude than the anterior lens in some higher order terms. On average, for the unaccommodated state, the individual dominant high-order irregularities of the anterior lens surface were horizontal/vertical (H/V) astigmatism (Z_2^{-2}), oblique trefoil (Z_3^{-3}), and spherical (Z_4^0), accounting for 15%, 11% and 21% of the variance, respectively. For the posterior lens surface, the individual dominant high-order irregularities were oblique astigmatism (Z_2^{-2}) and vertical quadrafoil (Z_4^4), accounting for 48% and 32% of the variance, respectively. The RMS of high-order irregularities and astigmatism of the posterior lens surface was statistically significantly higher than that of the anterior lens surface (high-order irregularities: $\times 2.02$, $p < 0.0001$; astigmatism: $\times 1.58$, $p = 0.01$).

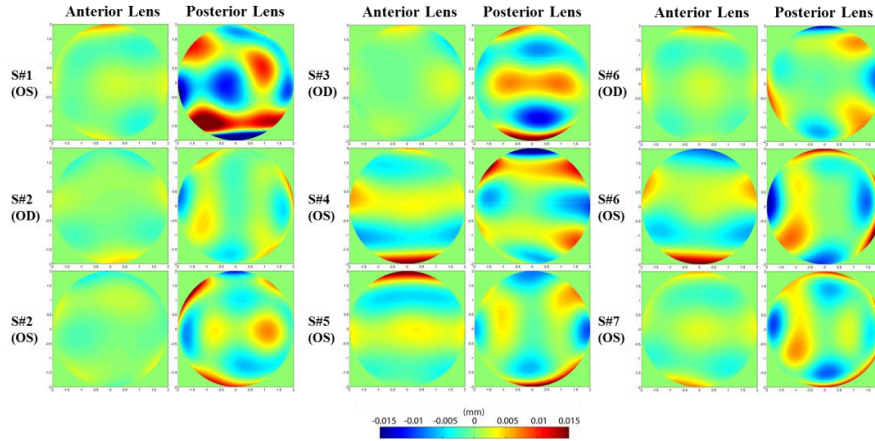


Fig. 4. Anterior and posterior crystalline lens elevation surface maps in the unaccommodated state (maps exclude tilt, defocus and astigmatism).

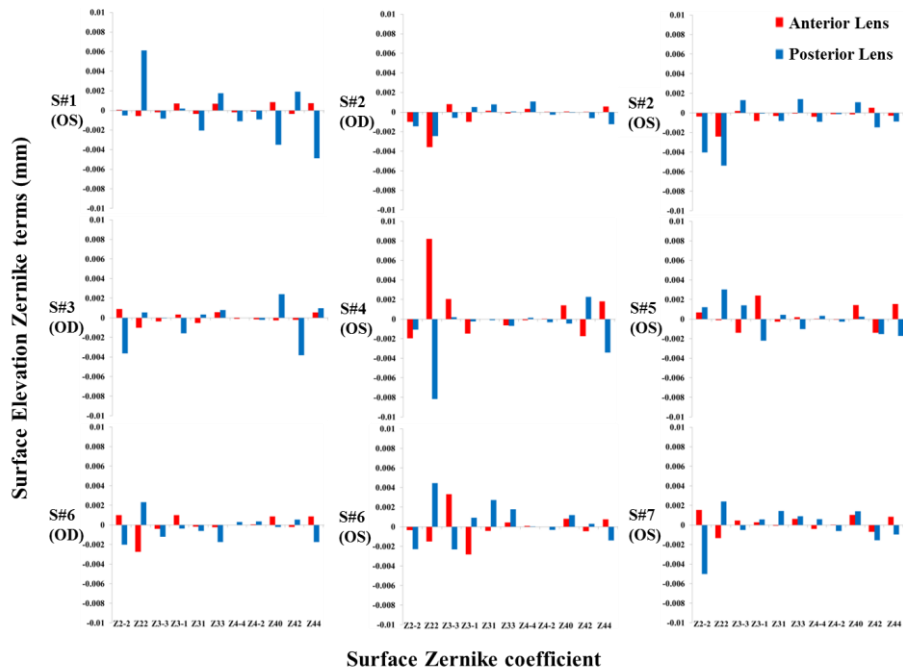


Fig. 5. Anterior and posterior crystalline lens surface Zernike coefficient (plots include astigmatism and high-order terms; pupil diameter is 4-mm).

3.2. Comparison of Zernike coefficients of ocular surfaces (cornea and crystalline lens)

An analysis of repeatability showed highly reproducible Zernike coefficient across repetitive measurements (average SD for all high-order Zernike coefficients) within each surface: 0.33 μm (anterior cornea), 0.57 μm (posterior cornea), 0.29 μm (anterior lens), 0.59 μm (posterior lens), in the relaxed state. Table 2 shows correlations of anterior and posterior corneal and anterior and posterior crystalline lens Zernike coefficients in the relaxed state. A significant correlation indicates that the magnitudes of individuals Zernike coefficients are closely associated. We found strong positive correlation in H/V astigmatism (Z_2^2), spherical (Z_4^0), vertical coma (Z_3^{-1}) and secondary astigmatism (Z_4^{-2})

and Z_4^2) between corneal surfaces, and strong negative correlation in vertical coma (Z_3^{-1}) and oblique trefoil (Z_3^{-3}) between lens surfaces. We further investigated the relationship between corneal and lens surfaces. There is significant positive correlation in the spherical aberration (Z_4^0) between anterior corneal and anterior lens surfaces and significant negative correlation in lateral coma (Z_3^1) and positive correlation in vertical trefoil (Z_3^{-3}) between anterior corneal and posterior lens surfaces.

Table 2. Pearson correlation coefficient and p-value for individual Zernike coefficients in corneal and lens surfaces in the relaxed state.

		<i>Cornea</i> <i>Ant vs Post</i>	<i>Lens</i> <i>Ant vs Post</i>	<i>Cornea & Lens</i>	
				<i>Ant Cornea vs</i> <i>Ant Lens</i>	<i>Ant Cornea vs</i> <i>Post Lens</i>
Astigmatism	Z_2^{-2}	r=0.55; p=0.15	r=-0.25; p=0.5	r=-0.57; p=0.1	r=-0.35; p=0.3
	Z_2^2	r=0.79; p=0.01*	r=0.63; p=0.08	r=-0.37; p=0.3	r=-0.37; p=0.3
Spherical	Z_4^0	r=0.79; p=0.02*	r=-0.34; p=0.41	r=0.83; p=0.01*	r=-0.19; p=0.6
Coma	Z_3^{-1}	r=0.69; p=0.05*	r=-0.74; p=0.03*	r=-0.39; p=0.3	r=0.53; p=0.16
	Z_3^1	r=0.39; p=0.33	r=0.06; p=0.87	r=-0.03; p=0.9	r=-0.73; p=0.03*
Trefoil	Z_3^{-3}	r=0.42; p=0.28	r=-0.71; p=0.04*	r=-0.33; p=0.4	r=0.82; p=0.01*
	Z_3^3	r=0.33; p=0.41	r=0.62; p=0.09	r=0.15; p=0.7	r=-0.26; p=0.5
Secondary	Z_4^{-2}	r=0.83; p=0.01*	r=0.28; p=0.49	r=-0.25; p=0.5	r=-0.35; p=0.3
Astigmatism	Z_4^2	r=0.97; p=0.001*	r=-0.33; p=0.38	r=0.42; p=0.3	r=-0.15; p=0.7

Figure 6(a) shows average Zernike coefficients of all subjects (astigmatism and high-order terms) of the corneal and lens surface elevation maps in the relaxed state. The higher corneal coefficients were the horizontal astigmatic terms Z_2^2 , followed by the spherical term Z_4^0 . Corneal surface astigmatism was significantly higher in the posterior than in the anterior cornea ($p < 0.001$). The sign of the average Zernike surface coefficients in the anterior and posterior crystalline lens surfaces is opposite in some coefficients (i.e. Z_2^2 , Z_3^{-1} , Z_3^{-3} and Z_4^4). As shown in Fig. 6(b), on average (all subjects) anterior and posterior corneal surfaces Zernike terms are positively correlated ($r = 0.97$, $p < 0.0001$), while anterior and posterior lens surfaces Zernike terms are negatively correlated ($r = 0.43$, $p = 0.04$).

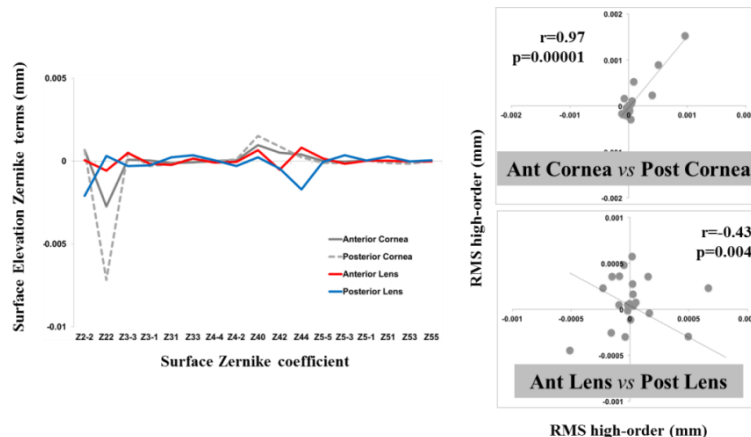


Fig. 6. (a) Cornea and crystalline lens surface elevation Zernike terms (astigmatism and high-order) in the relaxed state (average over all subjects). (b) Cornea and crystalline lens individual Zernike coefficients (high-order) in the relaxed state.

3.3. Phenylephrine vs natural anterior lens surface topography with accommodation

Figure 7 compares the Zernike coefficients of the anterior crystalline lens surface between phenylephrine and natural conditions, for different levels of accommodation. RMS differences range between 0.41 μm and 0.81 μm . The correlation between Zernike

coefficients of the lens surface elevation in both conditions were high ($r = 0.85-0.97$, $p < 0.0001$).

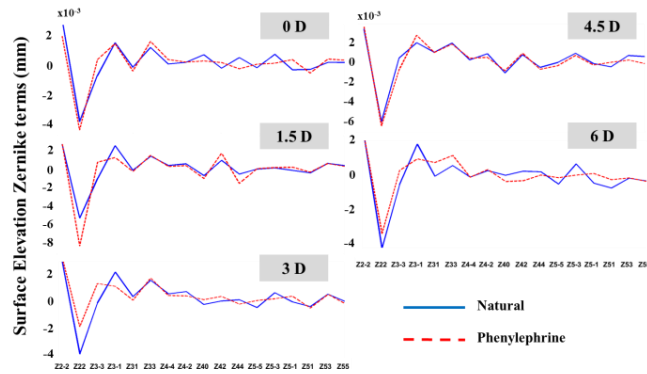


Fig. 7. Natural vs phenylephrine conditions in the anterior crystalline lens surface (Zernike coefficients) for all accommodative demands.

3.4. Changes in anterior segment geometry and biometry with accommodation

For the relaxed state, the average ACD was 3.43 ± 0.21 mm, central lens thickness was 3.88 ± 0.19 mm, and the average anterior and posterior lens radii of curvature were 13.07 ± 1.28 mm and -6.48 ± 0.51 mm respectively. ACD decreased at a rate of 0.04 ± 0.01 mm/D (Fig. 8(a)) and lens thickness increased at 0.04 ± 0.01 mm/D (Fig. 8(b)) with accommodative demand. Both anterior and posterior lens surfaces became steeper with accommodation (particularly the anterior lens surface): anterior and posterior lens radii of curvature changed at rates of 0.78 ± 0.18 and 0.13 ± 0.07 mm/D (Fig. 8(c) and 8(d)). The ranges of radii of curvature, ACD and lens thickness in the accommodated state, as well as their change with accommodative demand, are consistent with those reported in the literature [35]. On average, the standard deviation across subjects and accommodative states in axial distances were 0.028 mm in ACD and 0.027 mm in lens thickness. The optical power of the lens was estimated for all subjects at all accommodative demands (Fig. 8(e)). It ranges from 17.5 to 22.7 D in the relaxed state and from 21.5 to 25.9 D for 6 D of accommodative demand. The average change was 0.81 ± 0.19 D per D of accommodative demand.

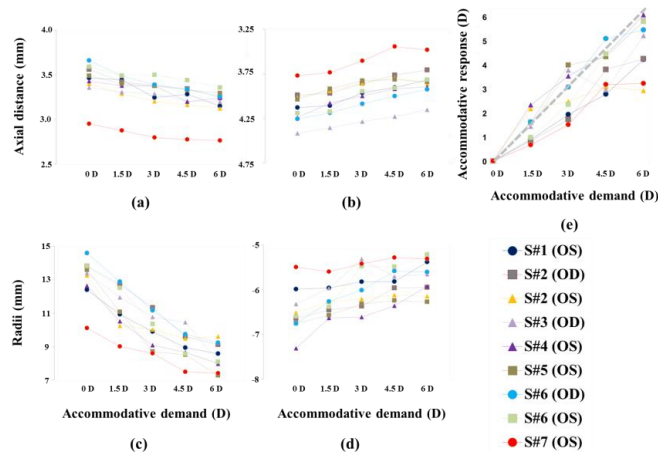


Fig. 8. Biometric and geometrical changes with accommodation: (a) Anterior Chamber Depth, (b) Lens Thickness, (c) Anterior Lens Radius and (d) Posterior Lens Radius (e) Accommodative response vs Accommodative demand in all subjects.

3.5. Changes in anterior and posterior lens surface elevation with accommodation

Figure 9 and [Visualization 1](#) shows an example (S#2, OS) of the corneal and lens segmented surfaces from the OCT image (left) and the corresponding anterior and posterior lens surface elevation maps for different accommodative states (right).

Figure 10 shows changes in RMS of high-order irregularities, astigmatism, coma, trefoil and spherical as a function of accommodative demands. High-order irregularities, astigmatism, coma and trefoil increased with accommodation by a factor of $\times 1.44$ ($p < 0.05$), $\times 1.95$ ($p < 0.05$), $\times 1.42$ and $\times 1.28$ in the anterior lens surface (between 0 and 6 D), respectively, and changed by a factor of $\times 1.04$, $\times 1.10$, $\times 1.39$ and $\times 1.33$ in the posterior lens surface (between 0 and 6 D), respectively. Interestingly, we found a notch at 3 D for the RMS high-order irregularities, RMS coma and RMS trefoil in 7/9 subjects in the posterior lens surface, but this was not found to be statistically significant. As in previous studies reporting wave aberrations, we found that the spherical term changed toward negative values with accommodation in the anterior lens surface but this tendency is not observed in the posterior lens surface.

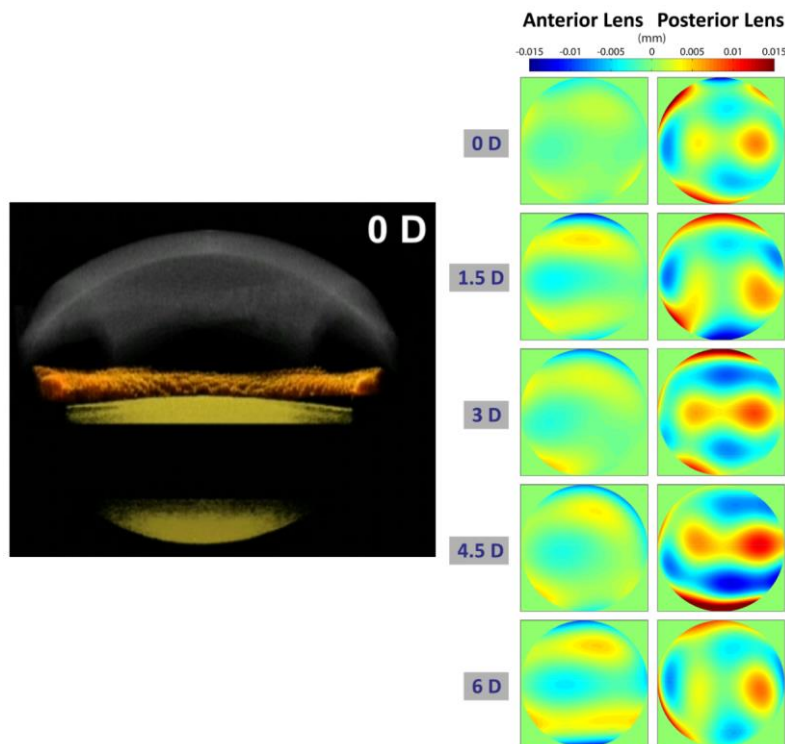


Fig. 9. ([Visualization 1](#)) Example of the anterior segment segmented surfaces (corneal and lens) with accommodation (left) and the corresponding lens surface elevation maps for different accommodative demands (right). Data are for subject S#2 (OS). Pupil diameter in maps is 4-mm.

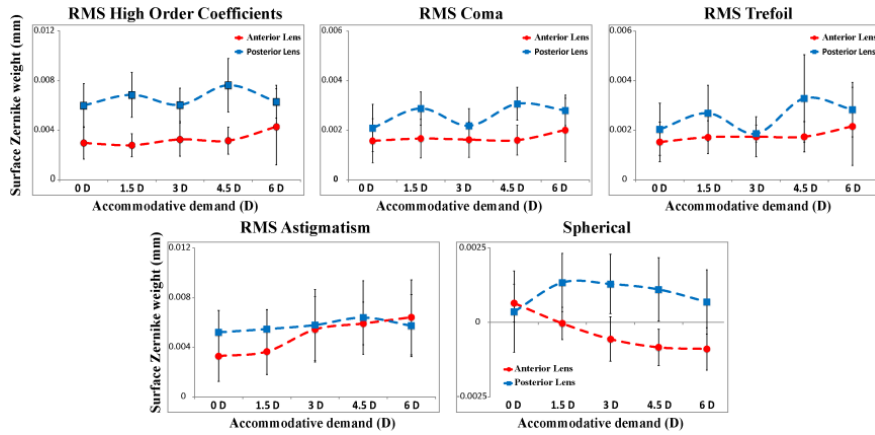


Fig. 10. Average RMS of high-order irregularities, astigmatism, coma, trefoil and spherical for different accommodative demands. Data are for 4-mm pupils.

Table 3 shows the average relative contribution (in terms of variance, RMS^2) of lower and higher order Zernike terms (astigmatism, coma, trefoil, spherical term, 4th order and of 5th and higher-order coefficients). In the relaxed state, the spherical term accounts for most of the surface irregularity in the anterior lens (47%). However, with accommodation, the astigmatism is the predominant surface irregularity (accounting for 90% of the variance). In contrast, the posterior lens surface astigmatism accounts for 70% of the variance in the relaxed state, but with accommodation its contribution decreased.

Table 3. Relative contribution (in terms of %) of different Zernike terms to the overall surface elevation maps (for 4-mm pupils).

	Anterior Lens Surface					Posterior Lens Surface				
	0 D	1.5 D	3 D	4.5 D	6 D	0 D	1.5 D	3 D	4.5 D	6 D
<i>Astigmatism</i>	17.05	93.16	91.03	94.05	94.52	70.06	48.13	21.20	3.33	68.67
<i>Coma</i>	3.12	5.35	2.76	0.46	0.53	1.33	0.10	7.47	3.59	13.10
<i>Trefoil</i>	13.13	0.67	1.96	0.06	0.06	2.45	6.85	14.88	0.31	3.07
<i>Spherical</i>	47.32	0.03	2.87	4.44	4.44	1.73	26.17	34.21	54.87	6.24
<i>4th order</i>	19.06	0.74	1.34	0.97	0.97	23.31	18.14	21.69	36.36	7.98
<i>Others</i>	0.30	0.03	0.01	0.01	0.01	1.11	0.58	0.53	1.51	0.91

3.6. Corneal and lens surface astigmatism magnitude and axes with accommodation

On average, the astigmatic axis of the anterior and posterior corneal surfaces tends to be aligned (6.2 ± 2.1 deg). In the relaxed state of accommodation, the astigmatic axis of the anterior lens surface is moderately rotated with respect to the anterior cornea (27 ± 25 deg, on average). Furthermore, the anterior and posterior lens astigmatism axes differed by 80 ± 42 deg.

Figure 11 shows a power vector analysis of surface astigmatism in anterior and posterior lens surface in all eyes, for all accommodative demands. Individually, the relative angle between corneal astigmatic axis and anterior lens astigmatic axis was <20 deg in 5/9 eyes (S#1 (OS), S#2 (OS), S#3 (OD), S#6 (OD) and S#6 (OS)), >20 and <50 deg in 3/9 eyes (S#2 (OD), S#5 (OS) and S#7 (OS)) and >80 deg in 1/9 eyes (S#4 (OS)). In contrast, the relative angle between the anterior and posterior lens was around 90 deg in 7/9 eyes (S#1 (OS), S#3 (OS), S#4 (OS), S#5 (OS), S#6 (OD), S#6 (OS) and S#7 (OS)), while was <10 deg in 2/9 eyes (S#2 and S#3). At the maximum accommodative demand the relative angle between anterior and posterior lens was on average 90 ± 43 deg, around 40 deg in 3/9 eyes (S#2 (OD), S#2 (OS) and S#4 (OS)), around 90 deg in 3/9 eyes (S#1 (OS), S#6 (OS) and S#6 (OS)) and >120 deg in 3/9 eyes (S#3 (OD), S#5 (OS) and S#7

(OS)). The average change of the astigmatism angle with accommodation was 15 ± 11 deg and 21 ± 18 deg in the anterior and in the posterior lens surface, respectively.

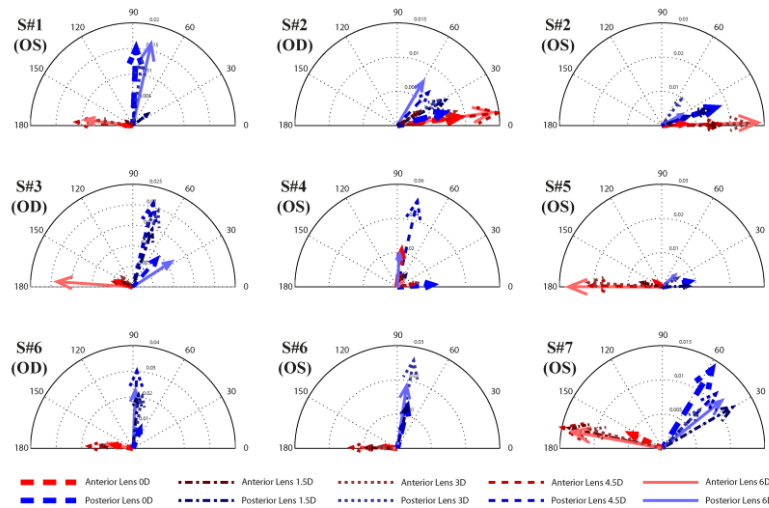


Fig. 11. Power vector polar plot of astigmatism in anterior and posterior crystalline lens surfaces, for different accommodative demands. Each panel represents a different eye. Red lines stand for anterior lens and blue lines for posterior lens astigmatism. Each line type represents a different accommodative demand. The angle represents the axis of astigmatism and the length of the vectors represents the magnitude of the corresponding surface astigmatism.

Figure 12 shows the change in the magnitude of astigmatism with accommodative demand. In the relaxed state, the magnitude of astigmatism was higher in the posterior lens surface but this tendency reversed in most subjects with accommodation.

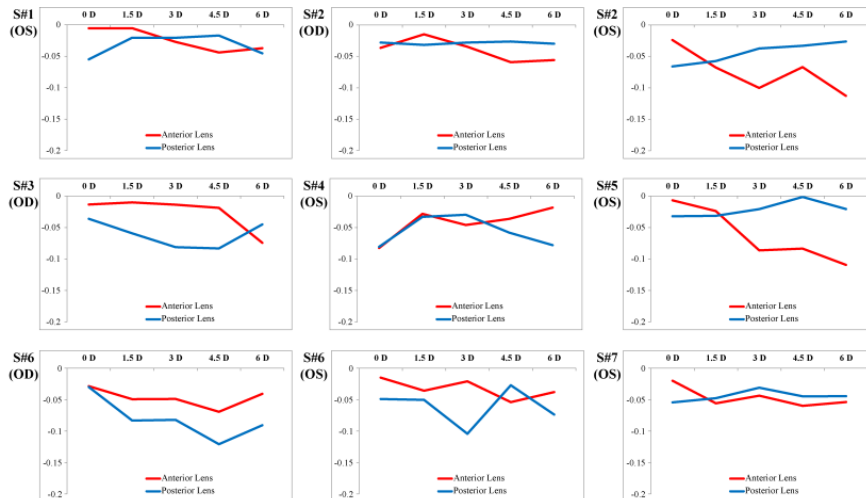


Fig. 12. Astigmatism surface magnitude in all eyes for different accommodative demands.

4. Discussion

The higher speed and axial and lateral resolution of OCT makes it an ideal tool to evaluate the anterior segment of the eye (cornea and lens) in 3-D. Most previous studies quantifying lens geometry *in vivo* using different imaging modalities were limited to only one or two central cross-sections (2-D information) and generally report only central

thickness and radii of curvature [19–21]. However, the cornea and the crystalline lens surfaces are non-rotationally symmetric, therefore 3-D measurements are required. Recently, OCT combined with dedicated image processing algorithms provide accurate 3-D corneal [30,38–40] and lens [28] surface reconstructions after distortion correction.

This study represents, to our knowledge, the first *in vivo* study reporting the cornea and the crystalline lens shapes in 3-D as a function of accommodation, allowing studying relationships across the surfaces elevation maps, and the 3-D changes of the anterior and posterior crystalline lens surfaces with accommodation.

Knowledge of corneal and lens astigmatism and surface irregularities is critical for understanding the underlying optical causes for astigmatism, and the relative contribution of the different optical elements. To date, the contribution of the crystalline lens astigmatism to total astigmatism comes from indirect comparison of ocular astigmatism (measured by refraction or aberrometry), and corneal astigmatism (measured by keratometry or corneal topography) [25,41–43]. Javal postulated a relationship between corneal and refractive astigmatism, proposing a compensation of -0.5 D of against-the-rule corneal astigmatism by the internal optics. However, the Javal rule has been adjusted over time, either based on theoretical considerations or clinical data [41,42,44]. Artal et al. [24] and Kelly et al. [25] found significant negative correlation for anterior corneal horizontal/vertical total and internal astigmatism of the internal optics, suggesting at least a partial compensation for corneal astigmatism by the lens in a relaxed state.

Our results suggest that compensation of astigmatism does not only happen between the cornea and the crystalline lens but also between the lens surfaces of the ocular components. In agreement with prior work by Dubbelman et al. [45,46] we found that on average the posterior corneal surface compensated part of the irregularities of the anterior cornea, in particular astigmatism (31% [45] / 18% in the current study) and coma (from 3.5% [46] / 12% in the current study). As in the cornea, our study also revealed a high correlation between the magnitude of the irregularities of the anterior and posterior lens surfaces in coma and trefoil terms, indicating coordinated development. Although we did not find correlations between the magnitude of astigmatism of the anterior and posterior crystalline lens surfaces, the tendency in many subjects for orthogonal astigmatic axis in anterior and posterior lens (which we had also shown *in vivo* in a preliminary study on three young subjects) also indicates compensatory processes accounted by lens geometry. Interestingly, this tendency was also reported in some *ex vivo* eyes by Sun et al. [47] on isolated crystalline lenses, more frequently in younger than older lenses.

Our study did not directly address the presence of Gradient Index (GRIN) distribution in the lens, and its potential role in our findings. Siedlecki et al. [48] found that a homogeneous index could overestimate the posterior lens asphericity but not the posterior lens radius of curvature. Previous work on isolated lenses shows that GRIN plays in fact a major compensatory role for the spherical aberration [49,50], by shifting lens spherical aberration towards more negative values, and therefore compensating the spherical aberration of the cornea. With accommodation, de Castro et al. [49] found more negative aberration and a larger shift toward more negative values. However, although posterior lens surface shape estimation could have a benefit by increasing knowledge of the lens GRIN (especially in the spherical Zernike terms), it should be noted that the *ex vivo* GRIN distribution represents more closely values the GRIN in a maximally accommodated state and it is unlikely that GRIN plays a major role in non-rotationally symmetric aberrations. In fact, in a recent study on the impact of shape and GRIN on the astigmatism of isolated lenses, Birkenfeld et al. [22] found little influence of GRIN on the magnitude and axis of lens astigmatism.

Overall, our results of crystalline lens surface elevation *in vivo* hold similarities with those that we recently reported on *ex vivo* human donor lenses [47]. As in this study, we found significant correlations between anterior and posterior vertical coma and vertical

trefoil (*ex vivo* data showed correlations also in several other high order terms). However, we found *in vivo* significantly higher astigmatism and high-order irregularities in with the posterior lens surface than in the anterior lens surface, which was not reported *ex vivo*. Differences between results *in vivo* and *ex vivo* may be associated to the lack of zonular tension in the isolated lenses, which may be responsible for some of the irregularities in the posterior lens *in vivo*. In fact isolated lenses adopt its more accommodated form, and therefore, lens surface elevations from *ex vivo* data are more representative of accommodating lenses.

As the lens accommodates, many studies have demonstrated accommodation-induced changes in aberrations of the eye, which include changes in spherical aberrations, and to a lesser extent in astigmatism, coma, and trefoil [6,8,9,23]. The most relevant high order aberration change in the lens with accommodation is the negative shift of spherical aberration (due to changes in radii of curvature and asphericity, and to a lesser extent GRIN). Although some of these changes may be associated to some changes in lens tilt with accommodation [51], our results show that changes in lens surface astigmatism (including relative anterior/posterior astigmatic angle shifts between 10 and 20 deg) can also occur. We also found some systematic (not monotonic) changes in high order surface terms, coma and trefoil in particular, with accommodation, both for anterior and posterior lens surfaces.

In summary, quantitative OCT imaging in accommodating eyes has allowed us to evaluate changes in the anterior segment of the eye with accommodation, including 3-D corneal and lens surface elevation maps, allowing us to gain insights on the geometrical changes undergone by the eye with accommodation, and the relative contribution of the different lens surfaces to the optics of the eye, including astigmatism and high-order aberrations. Further studies on a larger population of different age and/or refractive profiles will allow gaining insights on the role of the crystalline lens on the age-dependent changes of the eye's optics.

Acknowledgments

This research has received funding from the European Research Council under the European Union's Seventh Framework Program (FP/2007-2013) / ERC Grant Agreement. [ERC-2011- AdC 294099]. This study was also supported by Spanish Government grant FIS2011-25637 and FIS2014-56643-R to SM. The authors indicate the following financial disclosure(s): Spanish patent P201130685: Procedure to calibrate and correct the scan distortion of an optical coherence tomography system, (Sergio Ortiz, Susana Marcos, Damian Siedlecki, and Carlos Dorronosoro).